

## Atomic force microscopy with a 12-electrode piezoelectric tube scanner

Yuen K. Yong, Bilal Ahmed, and S. O. Reza Moheimani

*School of Electrical Engineering and Computer Science, The University of Newcastle,  
University Drive, New South Wales 2308, Australia*

(Received 9 July 2009; accepted 21 January 2010; published online 4 March 2010)

This paper presents a piezoelectric tube scanner with a novel electrode pattern and describes how it may be used for simultaneous sensing and actuation. The electrodes are arranged such that the tube is driven in an antisymmetrical manner, resulting in a collocated system suitable for positive position feedback (PPF). A PPF controller is designed to damp the scanner's resonance. Piezoelectric strain-induced voltage is used as measurement. The device is then installed into an atomic force microscope to obtain open- and closed-loop images of a grating at 10, 15.6, and 31 Hz scan rates. The closed-loop images are noticeably superior to the open-loop images, illustrating the effectiveness of the proposed scanner when used simultaneously as a sensor and an actuator. © 2010 American Institute of Physics. [doi:10.1063/1.3314901]

### I. INTRODUCTION

The atomic force microscope (AFM) was invented in the 1980s by Binnig *et al.*<sup>1</sup> AFMs are capable of generating topological maps of material surfaces on an atomic scale. They promise breakthroughs in areas such as material science,<sup>2-5</sup> nanoparticle characterization,<sup>6</sup> bionanotechnology,<sup>7,8</sup> nano-indentation for high-density data storage systems,<sup>9,10</sup> and nanomachining.<sup>11</sup>

AFMs are dramatically different from other available forms of microscopy. They do not need a light source, electron beam, or lenses to generate an image. Furthermore, they can produce three-dimensional maps of material surfaces at extremely high resolutions. The central components of an AFM consist of a positioning scanner, a microcantilever with a sharp probe of a few atoms wide at one end, a laser source, and a position sensitive photodiode (PSD). The laser source in the scanning unit is focused at the free end of the microcantilever and the PSD captures the laser beam reflected by the cantilever (see Fig. 1). The AFM can be operated in contact or noncontact mode. When operated in contact mode, the microcantilever is brought in contact with the sample. The sample is moved in a raster pattern by actuating the scanner. This causes the cantilever to deflect due to the variations in the surface topology of the sample. This deflection in turn causes a variation in the intensity of the reflected beam captured by the PSD. Based on the changes recorded by the PSD, an image of the sample surface is generated by the AFM circuitry and software. When operated in noncontact mode, the probe is brought into close proximity (within a few nanometers) of the sample. The microcantilever is deliberately vibrated at a particular frequency. Changes in the vibration amplitude or frequency are used to detect the surface structure of the sample.

Piezoelectric tube scanners are commonly used in commercially available AFMs to move the sample in the three coordinates. Although flexure-based scanners emerged as an alternative to piezoelectric scanners,<sup>12-14</sup> the latter is still widely used due to their ease of installation into AFMs, low

cost, and wide availability. Due to the large length-to-diameter ratio of a tube, when it is fixed at one end its free end will experience a relatively low mechanical resonance frequency. This makes the tube susceptible to scan-induced vibrations.<sup>15</sup> During a typical raster scan, a triangular waveform is applied to the fast axis ( $x$ -axis) and a staircase or ramp signal is applied to the slow axis ( $y$ -axis) of the tube. The triangular waveform contains all odd harmonics of the fundamental frequency. Although the amplitude of these harmonics is attenuated by a factor of  $1/n^2$ , where  $n$  is the number of the harmonic, a fast triangular waveform (which is a requisite for high-speed scanning) can excite the tube's resonance. To avoid this, the fastest scan rate of an AFM is often limited to 1% of its scanner's first mechanical resonance frequency.<sup>16</sup> For a scanner with a resonance frequency of 500 Hz, this translates into a scan speed of no faster than 5 Hz. The scan rate of a tube scanner is also limited by nonlinearities inherent to the piezoelectric materials, namely, hysteresis and creep.<sup>15,17</sup> The primary objective of this work is to deal with scan-induced vibrations in a novel AFM scanner and to study its effect on the generated image.

A number of feedback control techniques have been proposed for vibration control of piezoelectric tube scanners. In these methods, the key idea is to flatten the frequency response of the system by damping its first resonant mode, and thus to allow for a faster scan. A controller that is particularly suitable for this purpose is the positive position feedback (PPF) controller.<sup>18</sup> A PPF controller has a simple structure, and thus is easy to implement. Furthermore, when implemented on a collocated system it guarantees closed-loop stability. This controller has been successfully implemented on various mechanical structures.<sup>19-22</sup> PPF controllers belong to the class of strictly negative imaginary systems, and are also known to be inherently stabilizing when implemented on a negative imaginary system, to which flexible structures with collocated sensors and actuators belong.<sup>23</sup> Other vibration control techniques, such as resonant control<sup>24</sup> and integral resonant control,<sup>12,25,26</sup> are known to provide significant

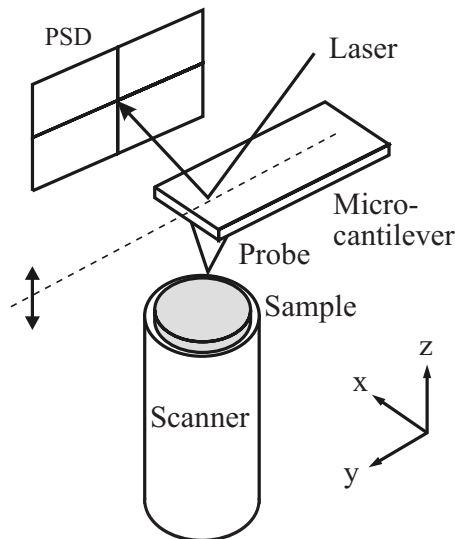


FIG. 1. Schematics of an AFM.

damping to highly resonant systems. Another straightforward and relevant control design approach is that of a polynomial-based controller.<sup>27</sup>

The main complication with the above feedback-based techniques is the need for a displacement sensor. As a result, the performance of a feedback system is dependent on the sensor noise and bandwidth. Capacitive sensors are commonly used for displacement measurement in high-precision positioning systems. These sensors typically have a rms noise of the order of  $20 \text{ pm}/\sqrt{\text{Hz}}$ .<sup>16</sup> This is clearly inadequate for scanning probe microscopy and other applications that require subnanometer precision.

Recently, a technique for simultaneous sensing and actuation of a piezoelectric tube was proposed in Refs. 20 and 21, where one of the tube's quartered electrodes is used for actuation and the opposite electrode is used for sensing. This is a rather attractive proposition since the noise density of piezoelectric strain-induced voltage was established to be three orders of magnitude lower than a typical capacitive sensor.<sup>16,28</sup> When operated in this mode, the tube is driven asymmetrically. Thus, its transfer function deviates from a perfectly collocated system. Furthermore, since only one electrode is used for actuation, the tube's range of motion is reduced by half. Two of the authors recently proposed a new electrode pattern for piezoelectric tube scanners that allows for simultaneous sensing and actuation.<sup>29</sup> The proposed tube scanner avoids the aforementioned complications associated with quartered electrode tubes. Compared to a quartered electrode tube, the proposed device has a larger range of motion, when operated as an actuator, and a better signal to noise ratio, when used for simultaneous sensing.

This paper illustrates how the proposed scanner can be modeled and controlled to allow for fast raster scans. Moreover, the controlled scanner is used as the scanning module of a commercial atomic force microscope to obtain high-quality images of a calibration grating at 10, 15.6, and 31 Hz scan rates.

The remainder of the paper is organized as follows. In Sec. II, we describe the proposed electrode pattern and the

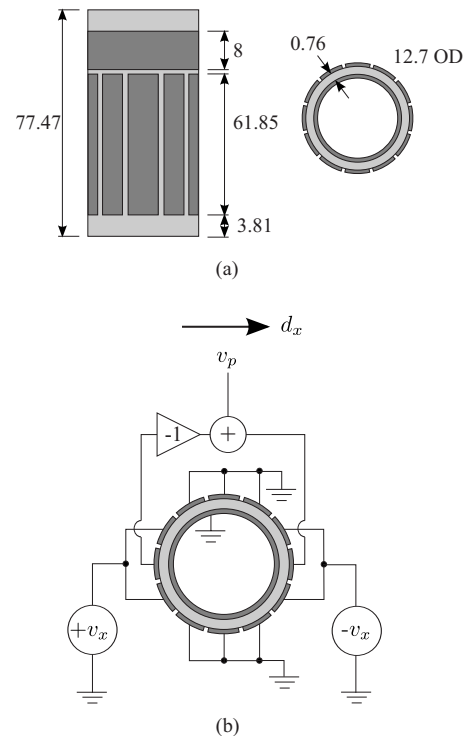


FIG. 2. Piezoelectric tube scanner. (a) Schematics of the proposed piezoelectric tube scanner with a 12-electrode pattern for  $x$  and  $y$  actuation and sensing. Light areas indicate piezoelectric material, and dark areas represent electrodes. All dimensions are in millimeter. (b) Electrodes wiring for actuation and sensing in the  $x$ -direction alone.  $v_x$  is the applied voltage and  $v_p$  is the piezoelectric strain-induced voltage.  $d_x$  represents the displacement measured at the end of the tube. Actuation and sensing in the  $y$ -direction can be achieved by wiring the appropriate electrodes in a similar way.

mechanical design of the scanner. Finite-element-analysis of the tube, simulating its static and dynamic characteristics, is performed in this section. Details of the tube scanner experimental setup are presented in Sec. III. Section IV describes the control design and implementation, characterization of sensor noise, and scan results obtained from the tube. Section V concludes the paper.

## II. THE 12-ELECTRODE PIEZOELECTRIC TUBE SCANNER

### A. Description of the tube scanner and the mechanical design

The schematics of our new piezoelectric tube scanner are shown in Fig. 2. The tube is made of PZT-5A piezoelectric material and was manufactured by Boston Piezo-Optics. It is poled radially outward. The external electrode is segmented into 12 equal sections of  $30^\circ$  each. It has a small continuous electrode at the top of the tube for  $z$ -axis actuation. The inside of the tube is covered by a continuous electrode which is grounded at all times. As shown in Fig. 3, one end of the tube scanner is fixed to a base bracket which is mounted to an aluminum casing in order to protect the tube. The assembled tube, base bracket, and casing are then mounted on a holder. A sensing target, which also serves as a stage over which a sample can be placed, is glued to the free end of the tube.

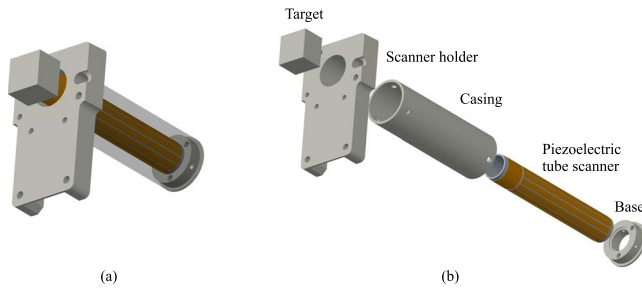


FIG. 3. (Color online) Computer aided design drawings of the scanner. (a) Assembly view. (b) Exploded view.

The electrode pattern design of the tube is tailored for simultaneous sensing and actuation.<sup>29</sup> Figure 2(b) illustrates the wiring of the tube for actuation and sensing in the  $x$ -axis alone. The arrangement for the  $y$ -direction sensing and actuation is similar and is not illustrated for brevity. The two outer electrodes on opposite sides are used for actuation. When voltages with equal magnitude but opposite polarity are applied to the opposite electrodes, one side of the tube extends and the opposite side retracts, resulting in bending. The strain experienced on each side of the tube is translated into a voltage at the respective central electrode due to the piezoelectric effect. Due to the symmetry, the voltages induced at the opposite electrodes are equal in magnitude but  $180^\circ$  out of phase. The voltage induced in one electrode is inverted and added to that obtained from the opposite electrode. The resulting signal is then used as an indication of the tube's deflection. Actuation and sensing in the  $y$ -direction can be obtained in a similar manner. For  $z$ -axis actuation, a voltage is applied to the continuous electrode ( $z$ -electrode) near the free end of the tube.

## B. Finite-element-analysis of the scanner

A finite-element (FE) model of the tube scanner was constructed in order to analyze its static and dynamic behavior. The following linear constitutive equations in a strain-charge form that describes the piezoelectric properties of the tube are used to generate the FE model.<sup>30,31</sup>

$$\mathbf{S} = \mathbf{s}^E \mathbf{T} + \mathbf{d} \mathbf{E}, \quad (1)$$

$$\mathbf{D} = \mathbf{d} \mathbf{T} + \boldsymbol{\epsilon}^T \mathbf{E}.$$

Here,  $\mathbf{S}$  is the strain vector,  $\mathbf{s}^E$  is the elastic compliance matrix,  $\mathbf{T}$  is the stress vector,  $\mathbf{d}$  is the piezoelectric constant matrix,  $\mathbf{E}$  is the electric field vector,  $\mathbf{D}$  is the electric displacement vector, and  $\boldsymbol{\epsilon}$  is the permittivity matrix.

The FE model is constructed using three-dimensional elements (SOLID5) in ANSYS. Nodes spread over the area of an electrode are fully coupled. Thus, they have the same degree-of-freedom (i.e., voltages). Our objectives are to ensure that the chosen tube scanner provides: (i) a high first resonance frequency for high-speed scanning, (ii) a relatively large displacement range, and (iii) the capability of providing sufficient piezoelectric strain-induced voltages ( $v_p$ ) for obtaining a good signal-to-noise ratio during measurement. The piezoelectric material PZT-5A is chosen for fabricating the tube scanner and its properties are listed in Table I. The tube dimensions are shown in Fig. 2.

Figure 4 shows the mode shapes of the tube with a sensing target mounted on top. To simplify the FE model, the simulated results were recorded without incorporating the mass of a sample, sample holder, and magnet. There are two identical bending and circumferential modes, each observed in the  $x$ - and  $y$ -axes, respectively. For brevity, only modes corresponding to the  $x$ -axis are shown in Fig. 4. The first, third, and eighth resonant modes are bending modes occurring at 658.4, 4.65, and 10.9 kHz, respectively. At 4.06 and

TABLE I. Material properties of piezoceramic PZT-5A (Ref. 32).

| Property                  | Data   |
|---------------------------|--|
| Elastic compliance matrix | $\mathbf{s}^E = \begin{bmatrix} 15.0 & -5.74 & -7.22 & 0 & 0 & 0 \\ -5.74 & 15.0 & -7.22 & 0 & 0 & 0 \\ -7.22 & -7.22 & 18.8 & 0 & 0 & 0 \\ 0 & 0 & 0 & 47.5 & 0 & 0 \\ 0 & 0 & 0 & 0 & 47.5 & 0 \\ 0 & 0 & 0 & 0 & 0 & 44.3 \end{bmatrix} \times 10^{-12} \text{ (m}^2/\text{N)}$ |
| Piezoelectric coupling    | $\mathbf{d} = \begin{bmatrix} 0 & 0 & 0 & 0 & 585 & 0 \\ 0 & 0 & 0 & 585 & 0 & 0 \\ -171 & -171 & 374 & 0 & 0 & 0 \end{bmatrix} \times 10^{-12} \text{ (m/V)}$   |
| Relative permittivity     | $\boldsymbol{\epsilon}/\epsilon_0 = \begin{bmatrix} 1730 & 0 & 0 \\ 0 & 1730 & 0 \\ 0 & 0 & 1700 \end{bmatrix}, \epsilon_0 = 8.854 \times 10^{-12} \text{ (F/M)}$  |
| Density                   | $\rho = 7500 \text{ kg/m}^3$   |

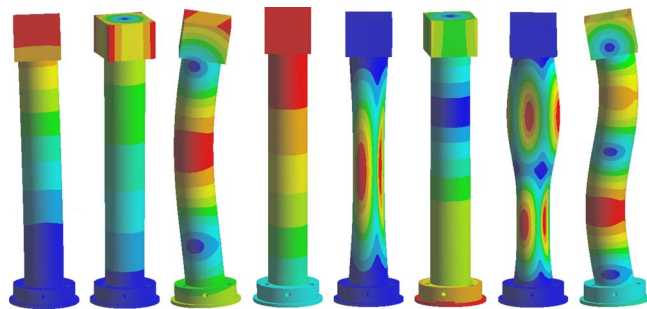


FIG. 4. (Color online) ANSYS simulated mode shapes of the scanner (without sample mass). The casing of the scanner is hidden in order to display the mode shapes clearly. From the left, first bending mode: 658.4 Hz, first torsional mode: 4.06 kHz, second bending mode: 4.65 kHz, first longitudinal extension mode: 5.76 kHz, first circumferential mode: 9.25 kHz, second torsional mode: 10.51 kHz, second circumferential mode: 10.77 kHz, and third bending mode: 10.9 kHz.

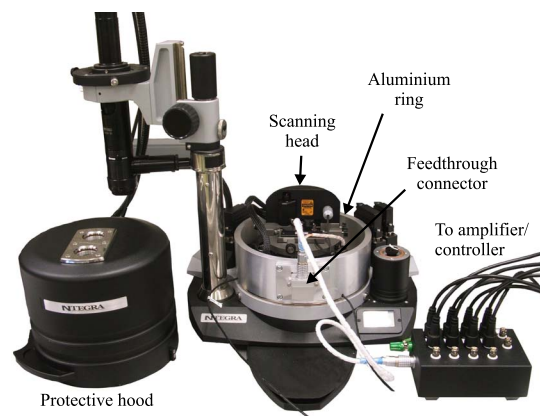
10.5 kHz, the respective first and second torsional modes of the tube are observed. The longitudinal extension mode occurs at 5.76 kHz. The first and second circumferential modes are observed at 9.25 and 10.77 kHz, respectively.

Assuming the system is linear, the static (dc) gain of the tube is estimated to be  $d_x/v_x=0.0724 \mu\text{m}/\text{V}$ . The sensitivity of the tube is estimated by recording the displacement of the sample holder in relation to the piezoelectric strain-induced voltage, i.e.,  $v_{p_x}/d_x=0.2 \text{ V}/\mu\text{m}$ . When an input voltage of 300 V is applied, the tube is displaced by 21.7  $\mu\text{m}$ . This amounts to  $v_{p_x}=4.3 \text{ V}$ , providing a good measurement signal for sensing. Gains of both the  $x$ - and  $y$ -axes are the same due to the symmetry. For  $z$ -axis actuation, the static (dc) gain of the tube is estimated to be  $d_z/v_z=1.97 \text{ nm}/\text{V}$ , where  $v_z$  is the voltage applied to the  $z$ -electrode. The tube provides a  $z$ -displacement of 0.6  $\mu\text{m}$  when 300 V is applied to this electrode. The  $z$  range is sufficient for atomic force microscopy.

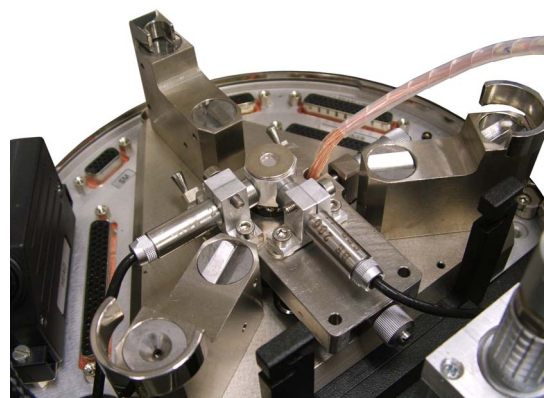
### III. SYSTEM DESCRIPTION AND EXPERIMENTAL SETUP

Figure 5 shows the NT-MDT NTEGRA scanning probe microscope (SPM) used to perform experiments reported here. This SPM is capable of performing scans in air and liquid. The SPM software limits the image resolution relative to scanning speed. At the highest resolution ( $256 \times 256$  scan lines) the fastest achievable scanning frequency is limited to 31 Hz. The scanning frequency can be increased by reducing the image resolution.

The SPM is configured to operate as an AFM. All scans presented in this work were performed in air. The original scanner of the SPM was replaced by the proposed tube scanner [see Fig. 5(b)]. A protective hood was used as a shield against acoustic noise, electromagnetic fields, and temperature variations. An aluminum ring was designed to serve as a base over which the protective hood was placed [see Fig. 5(a)]. A feedthrough connector was mounted into the ring to serve as a signal access unit to the scanner. This setup allows one to bypass the hood and to gain direct access to the electrodes of the scanner. The modified AFM system allows the tube scanner to be driven by external voltage amplifiers. This



(a)



(b)

FIG. 5. (Color online) Experimental apparatus. (a) A modified NT-MDT NTEGRA SPM. The tube scanner is located below the scanning head. (b) The tube scanner is installed into the SPM. The two capacitive sensors are mounted at right angles to the target.

modification also enabled us to implement a damping controller (to improve tube's resonant behavior) externally without the need for modifying the existing control logic of the AFM system.

The  $x$ - and  $y$ -axes of the tube were driven by a NANONIS bipolar high voltage amplifier HVA4. This amplifier has a maximum gain of 40 and a voltage range of  $\pm 400 \text{ V}$ . Piezoelectric strain-induced voltages have a first-order high-pass characteristic at low frequencies. This is due to the capacitive nature of the sensors and finite input impedance of the measurement device.<sup>28,33</sup> To minimize this characteristic, voltages measured at the central electrodes of the tube were fed to two low noise preamplifiers (Stanford Research Systems SR560). The input impedance of the preamplifier is 100 M $\Omega$ . The measured capacitance of each electrode is 3.2 nF. Together with the input impedance of 100 M $\Omega$  of the preamplifier, the cutoff frequency of the sensing signal is reduced to less than 1 Hz. The rms noise associated with the sensor was measured to be 0.25 nm. Since the electrodes are adjacent to each other, a small amount of electrical feedthrough from actuating electrodes to sensing electrodes is inevitable. This is due to the leakage of electric fields associated with actuating electrodes to piezoelectric material beneath the sensing electrode. However, the

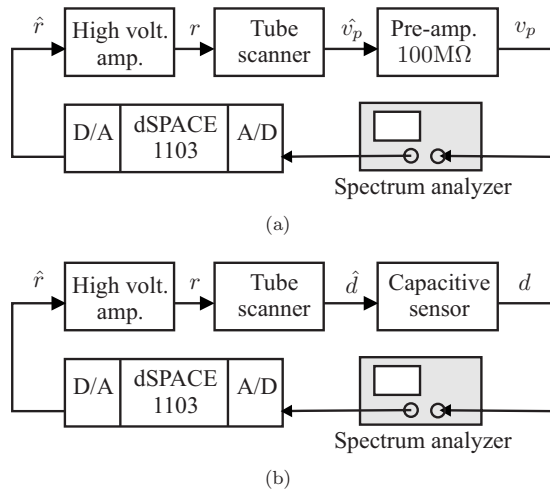


FIG. 6. Block diagrams of the experimental setup used for system identifications. (a) System identification of  $G_{vv}$ .  $\hat{r}$  is the reference input in volts, generated by the spectrum analyzer.  $r$  is the output of the voltage amplifier.  $\hat{v}_p$  is the strain-induced voltage of the tube scanner.  $v_p$  is the output voltage of the preamplifier. The FRF of  $G_{vv}$  plotted in Fig. 7 is from input  $r$  to output  $v_p$ . (b) System identification of  $G_{dv}$ .  $\hat{d}$  is the equivalent displacement of the tube in volts.  $d$  is the capacitive sensor output in micrometers. The FRF of  $G_{dv}$  plotted in Fig. 7 is from input  $r$  to output  $d$ .

feedthrough voltage is significantly smaller than the strain-induced voltage measured at the sensing voltage. Two ADE Technologies 8810 capacitive sensors were placed in close proximity to the adjacent surfaces of the sample holder to observe the displacements of the tube along the  $x$ - and  $y$ -axes [see Fig. 5(b)]. The static gain of the two sensors is  $2.5 \mu\text{m}/\text{V}$ .

The AFM controller was used to generate the  $x$  and  $y$  signals. These were accessed through the AFM signal access module and were applied to the controlled piezoelectric tube scanner through the high voltage amplifiers. A dSPACE-1103 rapid prototyping system was used to implement the  $x$ - and  $y$ -axes feedback controllers in real-time. The  $z$ -axis displacement was controlled using the AFM software and circuitry.

To design a controller for the scanner, one requires a dynamic model of the device. Such a model can be identified from the frequency response functions (FRFs) obtained from the apparatus. The FRFs of the scanner were obtained using a band-limited swept sine input of amplitude 200 mVpk, within the frequency range of 10 Hz to 10 kHz, and using a HP 35670A dual channel spectrum analyzer. In this case, the scanner was treated as a multivariable system. The two inputs are the voltages applied to the  $x$ - and  $y$ -axes amplifiers  $[v_x, v_y]^T$  while the outputs are the corresponding strain-induced voltages  $[v_{p_x}, v_{p_y}]^T$ , and displacements  $[d_x, d_y]^T$  of the tube measured by the capacitive sensors (see Fig. 6). The two measured subsystems, i.e.,  $G_{vv}(j\omega)$  and  $G_{dv}(j\omega)$ , are described as

$$Y_v(j\omega) \triangleq G_{vv}(j\omega)U(j\omega), \quad (2)$$

$$Y_c(j\omega) \triangleq G_{dv}(j\omega)U(j\omega), \quad (3)$$

where  $Y_v(j\omega)$  denotes the Fourier transforms of  $[v_{p_x}, v_{p_y}]^T$ ,  $Y_c(j\omega)$  denotes the Fourier transforms of  $[d_x, d_y]^T$ ,  $U(j\omega)$  de-

notes the Fourier transforms of the input voltage vector  $[v_x, v_y]^T$ , and

$$G_{vv}(j\omega) = \begin{bmatrix} G_{xx}(j\omega) & G_{xy}(j\omega) \\ G_{yx}(j\omega) & G_{yy}(j\omega) \end{bmatrix}, \quad (4)$$

$$G_{dv}(j\omega) = \begin{bmatrix} G_{d_x}(j\omega) & G_{d_y}(j\omega) \\ G_{d_x}(j\omega) & G_{d_y}(j\omega) \end{bmatrix}, \quad (5)$$

are  $2 \times 2$  matrices of the FRFs. The subscript  $vv$  in  $G_{vv}(j\omega)$  denotes that both the inputs and outputs are voltages, while the subscript  $dv$  in  $G_{dv}(j\omega)$  denotes that the inputs are voltages and outputs are displacements.

It can be observed from Fig. 7 that the two transfer functions  $G_{vv}(s)$  and  $G_{dv}(s)$  have identical poles. Therefore, a controller which provides the damping of  $G_{vv}(s)$  will have a similar effect on  $G_{dv}(s)$ .<sup>29</sup>

The FRFs in Fig. 7 were captured with a total mass of 4.3 g (i.e., the total mass of a sample, sample holder, and magnet) mounted on top of the tube. The first resonant peak appears at 499 Hz, which is 160 Hz less than the FE simulated result due to the additional mass. The second resonant mode was measured to be 4.2 kHz. The FE simulation (obtained without sample mass) shows that the second bending mode appears at 4.65 kHz. For comparison purposes, a small rectangular block with an equivalent mass of 4.3 g was incorporated into the FE model to simulate its effect on the system dynamics. This FE model predicts that the first and second resonant modes would appear at 530 Hz and 4.37 kHz, respectively, which are about 6% different from the experimental outcomes. The measured sensitivities of the tube,  $v_{p_x}/d_x = 0.17 \text{ V}/\mu\text{m}$ ,  $d_x/v_x = 0.0728 \mu\text{m}/\text{V}$ , and  $d_z/v_z = 2.1 \text{ nm}/\text{V}$ , are in close agreement with the FE simulations in Sec. II.

## IV. CONTROL DESIGN AND IMPLEMENTATION

### A. Control design

The main objective of this section is to design a feedback controller which will provide significant damping to  $G_{d_x}$ ,  $G_{d_y}$  by using  $v_{p_x}$ ,  $v_{p_y}$  as measurement signal, respectively. A PPF controller was designed and implemented to damp the first resonant mode of the  $x$ - and  $y$ -axes. The block diagram of the closed-loop system is shown in Fig. 8. The control scheme uses the induced voltages  $v_{p_x}$ ,  $v_{p_y}$  as the measurement for the PPF controllers, while the displacements  $d_x$ ,  $d_y$  are observed using the capacitive sensors.

For the purpose of control design, the cross couplings between the  $x$ - and  $y$ -axes were assumed to be negligible. The dynamics of the two axes are very similar. For brevity, only the  $x$ -axis controller design is discussed here. A controller for the  $y$ -axis was designed along similar lines. A second order model was fitted to the FRF data corresponding to  $G_{xx}$  (using the frequency domain subspace modeling technique)<sup>34</sup> to accurately capture the first dominant peak of the tube. The transfer function of the model obtained is

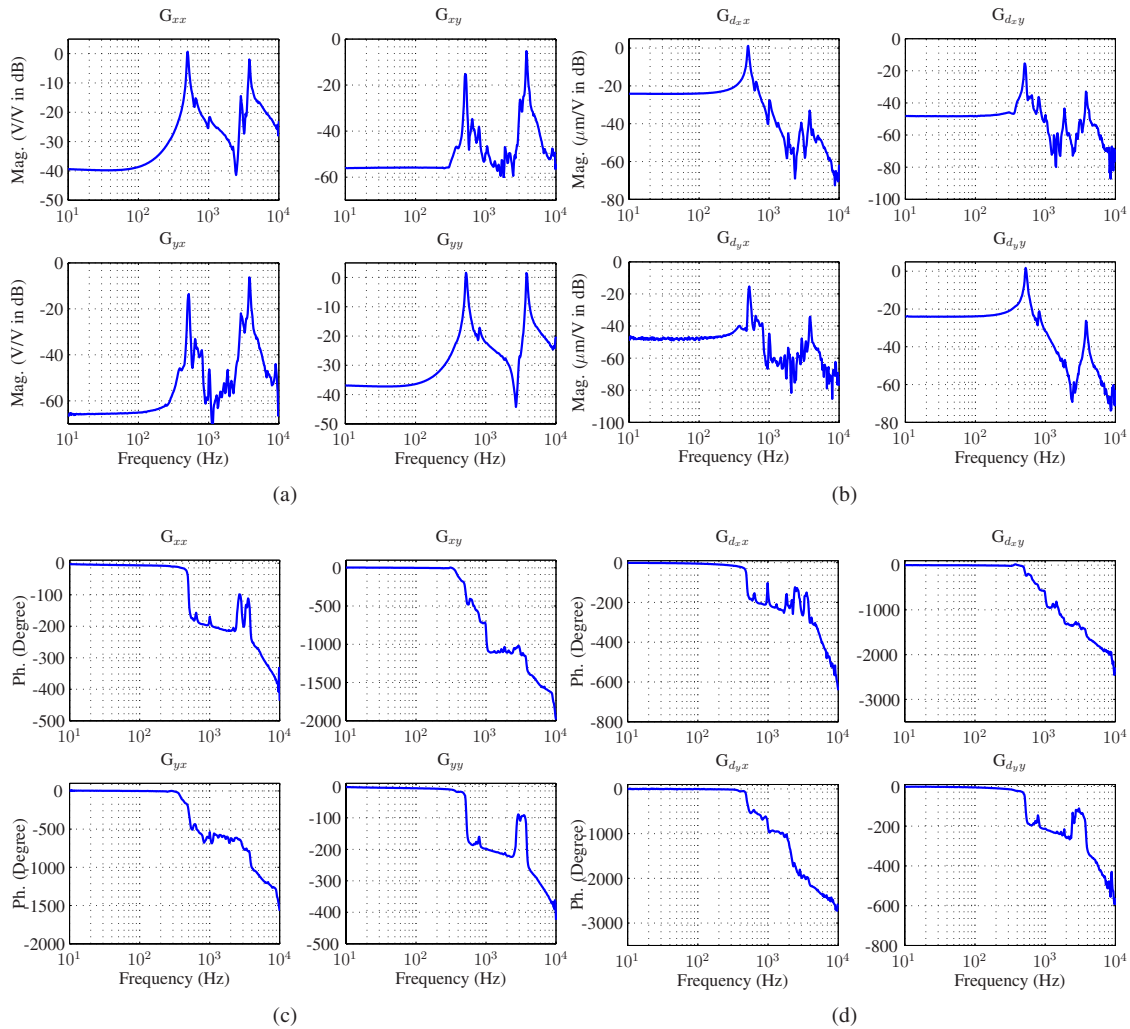


FIG. 7. (Color online) Measured open-loop FRFs of the tube scanner. (a) and (c) display the FRF of  $G_{vv}$ , plotted in magnitude (V/V in decibel vs hertz) and phase (degree vs hertz), respectively. (b) and (d) display the FRF of  $G_{dv}$ , plotted in magnitude ( $\mu\text{m}/\text{V}$  in decibel vs hertz) and phase (degree vs hertz), respectively.

$$G_{\text{model}}(s) = \frac{8.065 \times 10^6}{s^2 + 68.41s + 9.75 \times 10^6} - 0.6643. \quad (6)$$

Figure 9 shows the measured open loop frequency response  $G_{xx}(j\omega)$  and the identified model given in Eq. (6). It is evident that the estimated model provides a good fit for the nonparametric data in the frequency regions plotted. The proposed control law is elaborated in the following paragraphs.

Transfer function of  $G_{\text{model}}(s)$  in Eq. (6) can be written in time domain form as follows:<sup>20,21</sup>

$$\begin{aligned} \ddot{x} + 2\sigma\omega\dot{x} + \omega^2x &= \psi_1u, \\ y &= \psi_2x + du, \end{aligned} \quad (7)$$

where  $\psi_1 = 8.0657 \times 10^6$ ,  $\psi_2 = 1$ ,  $d = -0.6643$ ,  $\sigma = 1.095 \times 10^{-2}$ , and  $\omega = 3.1225 \times 10^3$ , see Eq. (6).

The control objective is to design a control law  $u$  for the system in Eq. (7) such that the closed-loop FRF would imply a well damped system. To achieve this objective, PPF control design technique<sup>18</sup> is used in this paper. The controller is defined as follows:

$$\ddot{z} + 2\zeta\eta\dot{z} + \eta^2z = \Gamma v_{p_x}, \quad (8)$$

where  $v_{p_x}$  is the input to the controller, and  $\zeta, \eta, \Gamma$  are the design parameters.

The input  $u$  in Eq. (7) is defined by

$$u(t) \triangleq z + r, \quad (9)$$

where  $r(t)$  is the reference signal and  $z(t)$  is the controller state. Substituting this in Eq. (7) we obtain

$$\ddot{x} + 2\sigma\omega\dot{x} + \omega^2x = \psi_1(z + r), \quad (10)$$

$$y = \psi_2x + d(z + r).$$

The controller input in Eq. (8) is set to

$$v_{p_x}(t) \triangleq y(t). \quad (11)$$

Substituting from Eq. (11) and expanding terms in Eq. (8), we get

$$\ddot{z} + 2\zeta\eta\dot{z} + (\eta^2 - \Gamma d)z = \Gamma(\psi_2x + dr). \quad (12)$$

Let

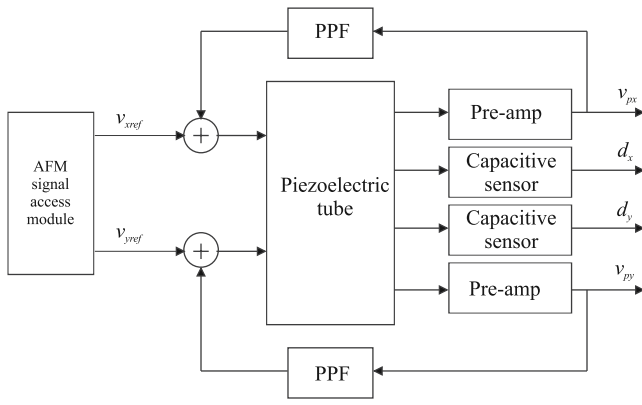


FIG. 8. Block diagram of the closed-loop system.  $v_{xref}$  and  $v_{yref}$  are the scanning reference waveforms provided by the AFM signal access module. The outputs  $v_{px}$  and  $v_{py}$  are used as inputs to the controller. The outputs  $d_x$  and  $d_y$  are the displacements of the tube scanner.

$$\rho \triangleq (\eta^2 - \Gamma d), \quad (13)$$

then Eq. (12) reduces to

$$\ddot{z} + 2\zeta\eta\dot{z} + \rho z = \Gamma(\psi_2 x + dr). \quad (14)$$

Equations (10) and (14) can be rewritten as follows:

$$\begin{bmatrix} \ddot{x} \\ \ddot{z} \end{bmatrix} + \begin{bmatrix} 2\sigma\omega & 0 \\ 0 & 2\zeta\eta \end{bmatrix} \begin{bmatrix} \dot{x} \\ \dot{z} \end{bmatrix} + \begin{bmatrix} \omega^2 & -\psi_2 \\ -\Gamma\psi_2 & \rho \end{bmatrix} \begin{bmatrix} x \\ z \end{bmatrix} = \begin{bmatrix} \psi_1 \\ \Gamma d \end{bmatrix} r(t), \quad (15)$$

$$y(t) = \begin{bmatrix} \psi_2 & d \end{bmatrix} \begin{bmatrix} x \\ z \end{bmatrix} + dr(t).$$

Taking the Laplace transform of Eq. (15) we get

$$\begin{bmatrix} s^2 + 2\sigma\omega s + \omega^2 & -\psi_1 \\ -\Gamma\psi_2 & s^2 + 2\zeta\eta s + \rho \end{bmatrix} \begin{bmatrix} x(s) \\ z(s) \end{bmatrix} = \begin{bmatrix} \psi_1 \\ \Gamma d \end{bmatrix} r(s), \quad (16)$$

$$y(s) = \begin{bmatrix} \psi_2 & d \end{bmatrix} \begin{bmatrix} x(s) \\ z(s) \end{bmatrix} + dr(s).$$

The closed loop poles of system in Eq. (16) are the roots of polynomial equation given by

$$P(s) \triangleq s^4 + (2\zeta\eta + 2\sigma\omega)s^3 + (\rho + 4\sigma\omega\zeta\eta + \omega^2)s^2 + (2\sigma\omega\rho + 2\zeta\eta\omega^2)s + \rho\omega^2 - \Gamma\psi_1\psi_2. \quad (17)$$

The PPF controller is designed to place the poles  $\{P_{ij}\}_{i=1}^4$  of Eq. (16) in a desired region of the left half plane. This design is achieved by choosing unknown parameters ( $\zeta, \eta, \Gamma$ ) in Eq. (17) such that

$$V = \sum_{k=1}^4 |P_k^d - \text{Re}(P_k^c)|^2 \quad (18)$$

is minimal.<sup>19</sup> The cost function in Eq. (18) minimizes the difference between the real part of the closed-loop poles  $\{P_k^c\}^4$  and the set of prespecified real values  $\{P_k^d\}^4$  in the left half plane.

Experiments were conducted on the scanner to demonstrate the practical application of the proposed controller.

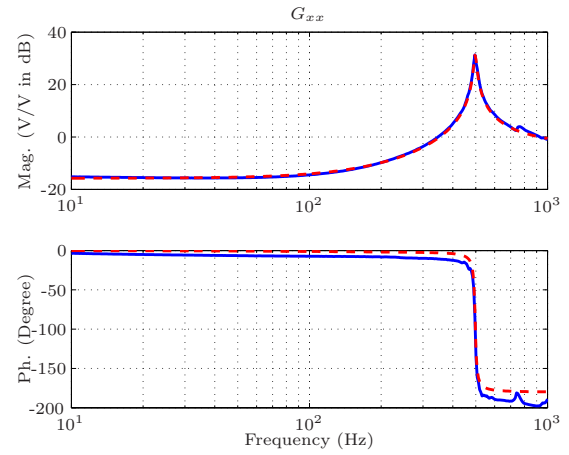


FIG. 9. (Color online) The identified second order model (---) along with the open-loop FRF of  $G_{xx}$  (-). The model captures the first resonant peak accurately.

The PPF controller was connected to the outputs  $v_{px}$ ,  $v_{py}$  to the inputs  $v_x$ ,  $v_y$  to damp the resonance in the systems  $G_{xx}$ ,  $G_{yy}$ , respectively. The experimental results are discussed below.

Open-loop poles of the transfer function  $G_{model}(s)$  are given by

$$P_{\pm} = -34.2 \pm i3.12 \times 10^3. \quad (19)$$

The PPF controller was designed in MATLAB/SIMULINK environment. The desired closed-loop pole locations were set further into the left half plane to impart sufficient damping in the closed-loop system. MATLAB function *lsqnonlin* was used to solve the optimization problem in Eq. (18). The actual closed-loop poles were found to be

$$P_{1+}^c = P_{2+}^c = -1.01 \times 10^3 \pm i2.31 \times 10^3, \quad (20)$$

$$P_{1-}^c = P_{2-}^c = -6.21 \times 10^2 \pm i3.39 \times 10^3.$$

Solving for the controller parameters  $\zeta, \eta, \Gamma$  from Eq. (8) using the cost function in Eq. (18), we obtain the PPF controller

$$K_{PPF}(s) \triangleq \frac{3.663 \times 10^6}{s^2 + 3202s + 8.337 \times 10^6}. \quad (21)$$

Figure 10 shows the measured open- and closed-loop FRFs of  $G_{vv}(j\omega)$  and  $G_{dv}(j\omega)$ . It is clear that the proposed controller for the system  $G_{vv}$  provides a similar effect on  $G_{dv}$ . It is evident from Fig. 10(b) that a damping of 21 dB is achieved at the dominant resonant mode using the PPF controller. The controller does not disturb the high frequency dynamics of the system. Furthermore, the experimental results show a significant damping in the cross-coupling terms.

## B. Characterization of sensor noise

A noise analysis of the piezoelectric strain-induced sensor is presented in this subsection. The open-loop noise data associated with the strain sensor was recorded when the piezoelectric tube scanner was stationary. The experiment was performed under controlled conditions, where external noise and vibrations were reduced to a minimum. Figure 11(a)

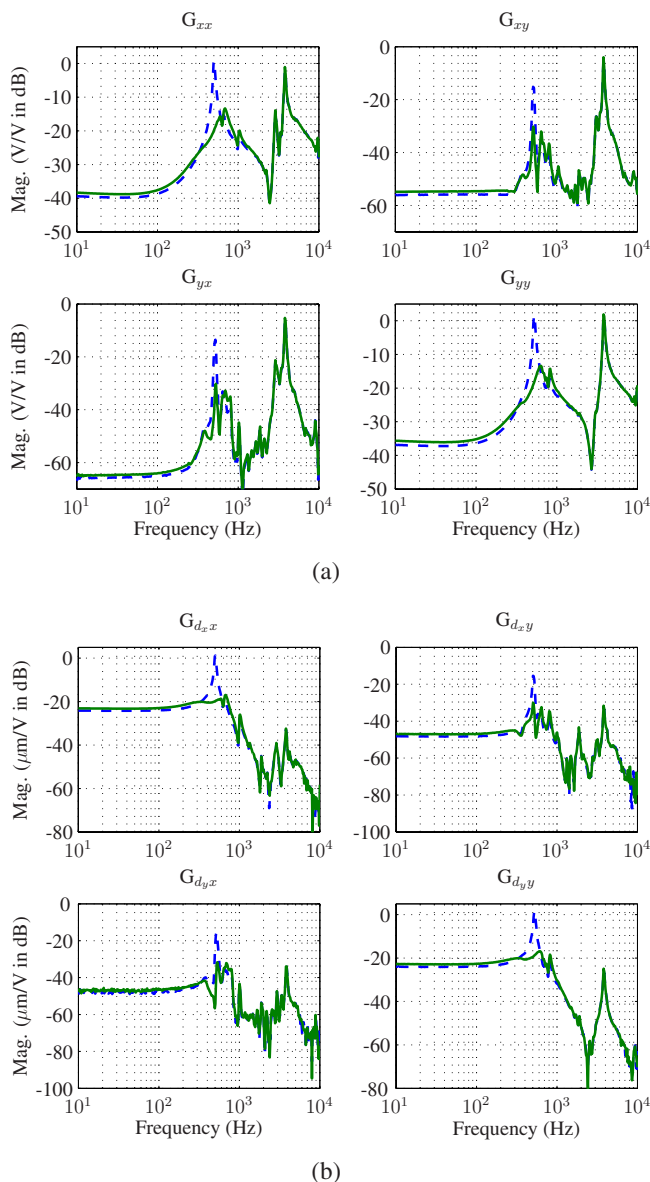


FIG. 10. (Color online) Closed-loop (-) gain response of  $G_{vv}$  (a) and  $G_{dv}$  (b) along with their open-loop counterpart (- -).

shows the open-loop measurement of the strain-induced sensor. The rms value of noise of the measurement open-loop noise is 0.25 nm, illustrating the sensor’s low-noise characteristics. In closed-loop, the sensor noise is fed back to the actuator. Therefore, in theory, the device resolution in closed-loop cannot achieve better resolution than that in open loop.<sup>35</sup> In order to analyze the effect of sensor noise on the scanner resolution, the following procedure was performed. A closed loop model was identified from the measured closed loop FRF using the subspace based modeling technique. The open-loop noise data were fed into the closed loop model to obtain the projected displacement of the piezoelectric tube scanner. The projected displacement provides an estimation of the “actual” displacement of the scanner which is below the sensor noise. Figure 11(b) shows the projected displacement of the scanner and its rms value. By using the strain-induced voltage as measurement, the resolution of the scanner is increased by a factor of 2. This es-

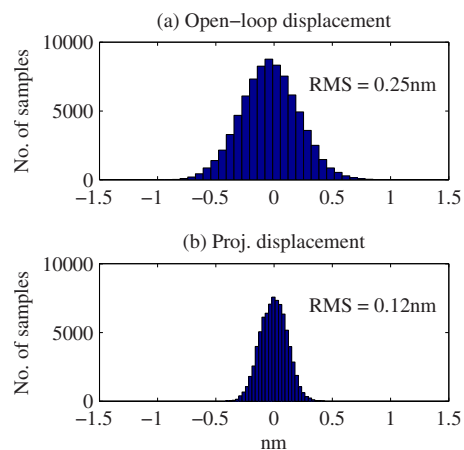


FIG. 11. (Color online) Open-loop measurement (top) and projected closed-loop displacement (bottom) of the strain-induced voltage sensor. The standard deviations  $\sigma$  are shown.

tablishes that the method proposed here does not lead to a situation where the sensor noise could adversely affect the tracking performance.

**C. Scan results**

In this section, scanned images of a calibration grating are used to evaluate the closed-loop performance of the tube scanner. Figure 12 shows the experimental configuration of the tube scanner for obtaining scans. A MikroMasch TGQ1 calibration grating with 3  $\mu\text{m}$  period, 1.5  $\mu\text{m}$  square side, and 20 nm height was used for experiments. A contact mode ContAl cantilever probe with a resonance frequency of 13 kHz was used to perform the scan. The vibration of the  $x$ - and  $y$ -axes are damped using the PPF controller. The  $z$ -axis displacement is controlled by the AFM in-built controller and voltage amplifier.  $10 \times 10 \mu\text{m}^2$  images (with  $256 \times 256$  scan lines) of the grating were recorded in constant height contact mode, in both open- and closed-loop at 10, 15.6, and 31 Hz scan rates.

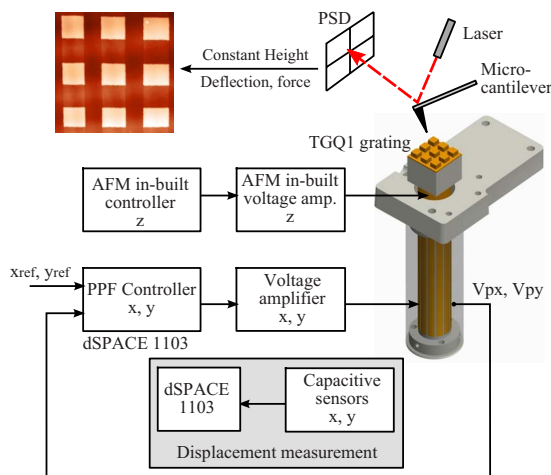


FIG. 12. (Color online) Experimental configuration of the scanner for generating scan images.

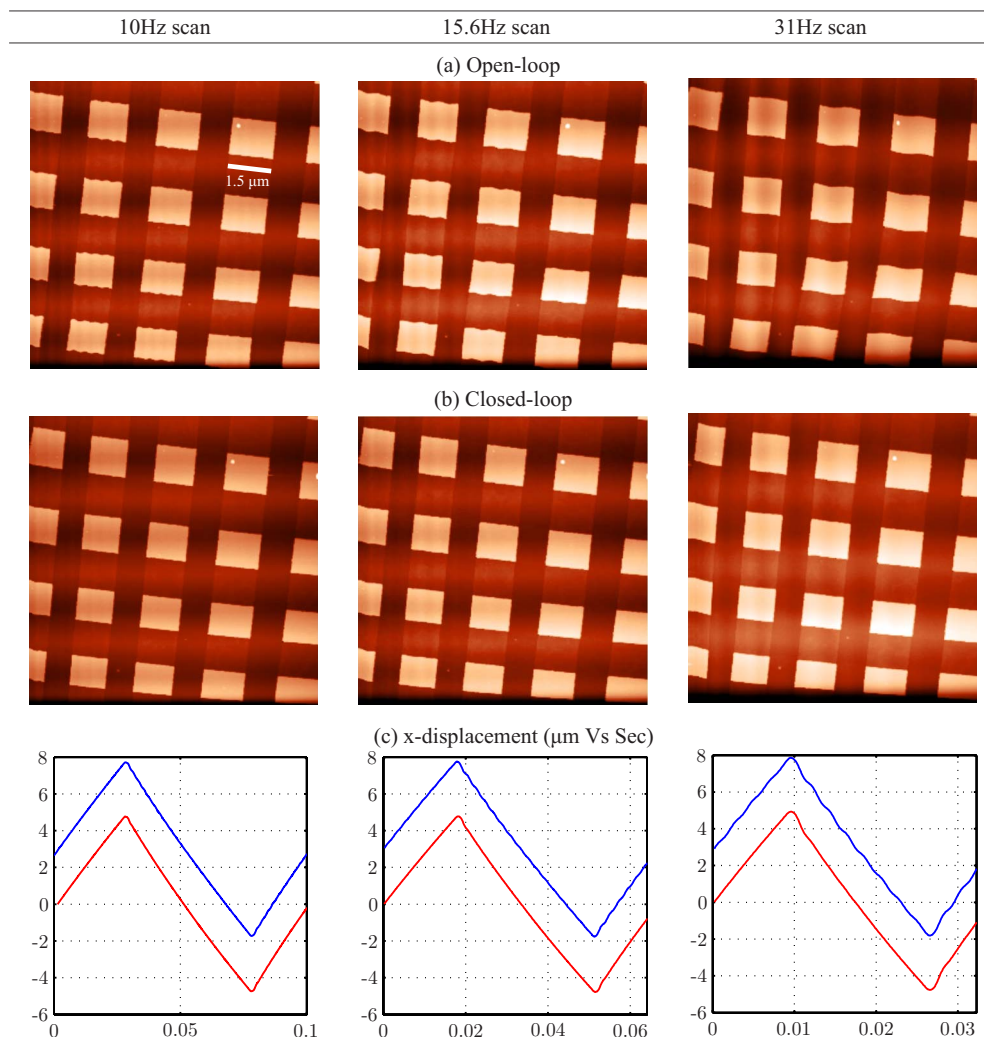


FIG. 13. (Color online) Recorded images ( $10 \times 10 \mu\text{m}^2$ ) of the grating at 10, 15.6, and 31 Hz. (a) Oscillations are clearly visible in the three open-loop scans. (b) Quality of the closed-loop scans (with the PPF controller activated) is noticeably improved compared with the open-loop scans. Oscillations are eliminated in the closed-loop scans. (c) Open- (with a positive offset) and closed-loop triangular waveforms are plotted. The hysteresis effect is minor but rather noticeable. Feedforward techniques and charge actuation methods can be used to reduce the hysteresis effect.

Figure 13 compares the open- and closed-loop images obtained from the modified AFM. At 10 Hz, the oscillation is visible in both the image and the measured  $x$ -axis displacement. The oscillation is suppressed when the PPF controller is activated.

Vibrations severely deteriorate the quality of the images at 15.6 and 31 Hz. The scanner vibrates at a higher magnitude at 31 Hz than at 10 and 15.6 Hz, but the image does not appear to be much more distorted. This is due to the fact that the magnitude of oscillation at 31 Hz is almost the same as the square side length of the image, i.e., a lower frequency harmonic is amplified by the tube resonance. With the controller activated, the oscillations are again eliminated.

The  $x$ - and  $y$ -axes were driven using a voltage amplifier and images were generated over a relatively large scan range. The hysteresis effect is minor but rather noticeable in both the images and measured  $x$ -axis displacements. Feedforward techniques, which do not require an on-line sensor, can be used to reduce the hysteresis effect.<sup>17,36,37</sup> A number of accurate hysteresis models, such as the Preisach models<sup>38,39</sup> and the Maxwell resistive capacitor model,<sup>40</sup> can be utilized in

conjunction with feedforward controls to minimize the presence of hysteresis. Alternatively, the scanner can be driven by charge amplifiers, which are known to linearize the piezoelectric actuators.<sup>12,41</sup>

## V. CONCLUSIONS

The use of a new type of piezoelectric tube scanner, with simultaneous sensing and actuation capabilities, for atomic force microscopy was studied in this paper. A FE model of the scanner was constructed in ANSYS to analyze its static and dynamic behavior. The obtained FE model suggests a good agreement with the experimental outcomes. A dynamic model of the scanner was then identified and, based on this model, a PPF controller was designed and implemented to improve its resonant behavior. Scan images of  $10 \times 10 \mu\text{m}^2$  were generated with the scanner operated both in open- and closed-loop, at 10, 15.6, and 31 Hz. Closed-loop images were observed to be much more superior to the open-loop images, implying the effectiveness of using strain-induced voltages in an AFM feedback system.

This paper presented the use of piezoelectric strain-induced voltages for damping in a 12-electrode piezoelectric tube scanner. Although the strain sensor is compact and can be easily fabricated, the high-pass characteristic of the sensor may cause the implementation of a tracking controller difficult. For future work, sensor fusion (a two-sensor-based method)<sup>16,28</sup> will be implemented on the 12-electrode tube scanner to achieve high accuracy tracking performance with low displacement noise.

## ACKNOWLEDGMENTS

This research was supported by the Australian Research Council Centre of Excellence for Dynamic Systems and Control.

- <sup>1</sup>G. Binnig, C. F. Quate, and C. Gerber, *Phys. Rev. Lett.* **56**, 930 (1986).
- <sup>2</sup>K. Miyahara, N. Nagashima, T. Ohmura, and S. Matsuoka, *Nanostruct. Mater.* **12**, 1049 (1999).
- <sup>3</sup>I. Schmitz, M. Schreiner, G. Friedbacher, and M. Grasserbauer, *Appl. Surf. Sci.* **115**, 190 (1997).
- <sup>4</sup>K. Yamanaka, A. Noguchi, T. Tsuji, T. Koike, and T. Goto, *Surf. Interface Anal.* **27**, 600 (1999).
- <sup>5</sup>S. Sundararajan and B. Bhushan, *Sens. Actuators, A* **101**, 338 (2002).
- <sup>6</sup>J. Scaff and P. West, "Part I: Introduction to nanoparticle characterization with AFM," <http://nanoparticles.pacificnanotech.com>, 2006.
- <sup>7</sup>T. Ando, N. Koder, D. Maruyama, E. Takai, K. Saito, and A. Toda, *Jpn. J. Appl. Phys., Part 1* **41**, 4851 (2002).
- <sup>8</sup>M. J. Rost, G. J. C. van Baarle, A. J. Katan, W. M. van Spengen, P. Schakel, W. A. van Loo, T. H. Oosterkamp, and J. W. M. Frenken, *Asian J. Control* **11**, 110 (2009).
- <sup>9</sup>P. Vettiger, G. Cross, M. Despont, U. Drechsler, U. Dürig, B. Gotsmann, W. Häberle, M. A. Lantz, H. E. Rothuizen, R. Stutz, and G. K. Binnig, *IEEE Trans. Nanotechnol.* **1**, 39 (2002).
- <sup>10</sup>A. Sebastian, A. Pantazi, S. O. R. Moheimani, H. Pozidis, and E. Eleftheriou, *IEEE Trans. Nanotechnol.* **7**, 586 (2008).
- <sup>11</sup>*Springer Handbook of Nanotechnology*, 2nd ed., edited by B. Bhushan (Springer, New York, 2004).
- <sup>12</sup>Y. K. Yong, S. Aphale, and S. O. R. Moheimani, *IEEE Trans. Nanotechnol.* **8**, 46 (2009).
- <sup>13</sup>S. Salapaka, A. Sebastian, J. P. Cleveland, and M. V. Salapaka, *Rev. Sci. Instrum.* **73**, 3232 (2002).
- <sup>14</sup>G. Schitter, K. J. Åstrom, B. DeMartini, P. J. Thurner, K. L. Turner, and P. K. Hansma, *IEEE Trans. Control Syst. Technol.* **15**, 906 (2007).
- <sup>15</sup>D. Croft, G. Shedd, and S. Devasia, *ASME J. Dyn. Syst., Meas., Control* **123**, 35 (2001).
- <sup>16</sup>A. J. Fleming, A. Wills, and S. O. R. Moheimani, *IEEE Trans. Control Syst. Technol.* **16**, 1265 (2008).
- <sup>17</sup>S. O. R. Moheimani, *Rev. Sci. Instrum.* **79**, 071101 (2008).
- <sup>18</sup>J. L. Fanson and T. K. Caughey, *AIAA J.* **28**, 717 (1990).
- <sup>19</sup>S. O. R. Moheimani, B. J. G. Vautier, and B. Bhikkaji, *IEEE Trans. Control Syst. Technol.* **14**, 443 (2006).
- <sup>20</sup>B. Bhikkaji, M. Ratnam, A. J. Fleming, and S. O. R. Moheimani, *IEEE Trans. Control Syst. Technol.* **15**, 853 (2007).
- <sup>21</sup>B. Bhikkaji, M. Ratnam, and S. O. R. Moheimani, *Sens. Actuators, A* **135**, 700 (2007).
- <sup>22</sup>G. Song and B. N. Agrawal, *Acta Astronaut.* **49**, 73 (2001).
- <sup>23</sup>A. Lanzon and I. R. Petersen, *IEEE Trans. Autom. Control* **53**, 1042 (2008).
- <sup>24</sup>H. R. Pota, S. O. R. Moheimani, and M. Smith, *Smart Mater. Struct.* **11**, 301 (2002).
- <sup>25</sup>S. S. Aphale, A. J. Fleming, and S. O. R. Moheimani, *Smart Mater. Struct.* **16**, 439 (2007).
- <sup>26</sup>B. Bhikkaji and S. O. R. Moheimani, *IEEE/ASME Trans. Mechatron.* **13**, 530 (2008).
- <sup>27</sup>G. C. Goodwin, S. F. Graebe, and M. E. Salgado, *Control System Design* (Prentice Hall, New York, 2001).
- <sup>28</sup>I. A. Mahmood, S. O. R. Moheimani, and K. Liu, *IEEE Trans. Nanotechnol.* **8**, 55 (2009).
- <sup>29</sup>S. O. R. Moheimani and Y. K. Yong, *Rev. Sci. Instrum.* **79**, 073702 (2008).
- <sup>30</sup>IEEE standard on piezoelectricity. ANSI/IEEE Std. 176–1987, 1988.
- <sup>31</sup>S. O. R. Moheimani, *IEEE Trans. Control Syst. Technol.* **11**, 482 (2003).
- <sup>32</sup>See Boston Piezo-Optics <http://bostonpiezooptics.com> for piezoceramic material properties.
- <sup>33</sup>S. O. R. Moheimani and A. J. Fleming, *Piezoelectric Transducers for Vibration Control and Damping* (Springer, Germany, 2006).
- <sup>34</sup>T. McKelvey, H. Akcay, and L. Ljung, *IEEE Trans. Autom. Control* **41**, 960 (1996).
- <sup>35</sup>A. Sebastian and S. M. Salapaka, *IEEE Trans. Contr. Syst. Technol.* **13**, 868 (2005).
- <sup>36</sup>Q. Zou, K. K. Leang, E. Sadoun, M. J. Reed, and S. Devasia, *Asian J. Control* **6**, 164 (2004).
- <sup>37</sup>S. S. Aphale, S. Devasia, and S. O. R. Moheimani, *Nanotechnology* **19**, 125503 (2008).
- <sup>38</sup>P. Ge and M. Jouaneh, *Precis. Eng.* **17**, 211 (1995).
- <sup>39</sup>R. B. Mrad and H. Hu, *IEEE/ASME Trans. Mechatron.* **7**, 479 (2002).
- <sup>40</sup>M. Goldfarb and N. Celanovic, *ASME J. Dyn. Syst., Meas., Control* **119**, 478 (1997).
- <sup>41</sup>A. J. Fleming and S. O. R. Moheimani, *Rev. Sci. Instrum.* **76**, 073707 (2005).